HHS Public Access

Author manuscript

IEEE Trans Med Imaging. Author manuscript; available in PMC 2020 May 04.

Published in final edited form as:

IEEE Trans Med Imaging. 2020 February ; 39(2): 468–477. doi:10.1109/TMI.2019.2928740.

Simultaneous Photoacoustic Imaging and Cavitation Mapping in Shockwave Lithotripsy

Mucong Li[1], **Bangxin Lan**[1], **Georgii Sankin**[2], **Yuan Zhou**[1], **Wei Liu**[1], **Jun Xia**[3], **Depeng Wang**[3], **Gregg Trahey**[1], **Pei Zhong**[2,*], **Junjie Yao**[1,*]

[1]Department of Biomedical Engineering, Duke University, Durham, NC 27708, USA.

[2]Department of Mechanical Engineering and Materials Science, Duke University, Durham, NC 27708, USA.

[3]Department of Biomedical Engineering, University of Buffalo, Buffalo, NY 14260, USA.

Abstract

Kidney stone disease is a major health problem worldwide. Shockwave lithotripsy (SWL), which uses high-energy shockwave pulses to break up kidney stones, is extensively used in clinic. However, despite its noninvasiveness, SWL can produce cavitation *in vivo*. The rapid expansion and violent collapse of cavitation bubbles in small blood vessels may result in renal vascular injury. To better understand the mechanism of tissue injury and improve treatment safety and efficiency, it is highly desirable to concurrently detect cavitation and vascular injury during SWL. Current imaging modalities used in SWL (*e.g.*, C-arm fluoroscopy and B-mode ultrasound) are not sensitive to vascular injuries. By contrast, photoacoustic imaging is a non-invasive and non-radiative imaging modality that is sensitive to blood, by using hemoglobin as the endogenous contrast. Moreover, photoacoustic imaging is also compatible with passive cavitation detection by sharing the ultrasound detection system. Here, we have integrated shockwave treatment, photoacoustic imaging and passive cavitation detection into a single system. Our experimental results on phantoms and *in vivo* small animals have collectively demonstrated that the integrated system is capable of capturing shockwave-induced cavitation and the resultant vascular injury simultaneously. We expect that the integrated system, when combined with our recently developed internal-light-illumination photoacoustic imaging, will find important applications for monitoring shockwave-induced vascular injury in deep tissues during SWL.

Keywords

Shockwave lithotripsy; kidney stone; vascular injury; photoacoustic imaging; hemorrhage monitoring; cavitation detection

I. INTRODUCTION

Kidney stone disease is a major health problem with substantial costs and disruption to patients' lives [1–4]. About 22.1 million cases occurred worldwide in 2015, resulting in

*P. Zhong, pzhong@duke.edu, J. Yao, junjie.yao@duke.edu.

about 16,100 deaths [5]. In the U. S., about 9% of the population will have an episode of kidney stone during their lifetimes with the direct medical treatment expenditures exceeding $2 billion annually [6]. Shockwave lithotripsy (SWL) is a treatment technique that uses high-energy shockwave pulses to break the stones in the kidney or peripheral organs such as ureter. With its non-invasiveness, ease of use, and high reimbursement rate, shockwave lithotripsy (SWL) has remained as the first-line therapy for the management of stone patients despite the advancements in ureteroscopy and laser lithotripsy [7–9]. In SWL, two types of mechanical force contribute to the stone comminution: the internal tensile and shear stress, and the external cavitation [10, 11]. The internal tensile and shear stress produces strong compression inside the stone and fractures the stone into smaller pieces. The shockwave-induced external cavitation forms bubbles surrounding the stone fragments [10, 12], and the violent bubble collapse leads to secondary shockwaves that can further grind down the stones [12, 13].

The same mechanical forces that comminute stones, however, also contribute to renal injuries [14–16]. It has been widely reported that SWL-induced injuries range from self-limited trauma to potentially life-threatening complications [17–19]. In particular, with much increased output acoustic pressure, contemporary lithotripters have high propensity for renal vascular injuries [20, 21]. For example, a clinical dose of 2000 shocks using the maximum output energy and pulse repetition rate on an HM3 lithotripter can produce a parenchymal lesion measuring ~6% of the functional renal volume [22]. Post-SWL, about 100% patients experience mild hematuria, up to 29% patients develop hematomas, and in rare cases, excessive bleeding can develop [23–25]. In severe cases, the injury is catastrophic, leading to permanent renal damage or even death [26].

In clinical SWL, C-arm fluoroscopy is used alone or in combination with B-mode ultrasound for stone localization and treatment monitoring. However, neither imaging modality is sensitive to vascular injuries [27]. Although visualization of blood vessels by B-mode ultrasound can be enhanced by ultrasound contrast agents (*i.e.*, encapsulated microbubbles), the delivered microbubbles can potentially cause damages during SWL treatment as they serve as cavitation nuclei in the vasculature and thus greatly increase the risk of bleeding upon subsequent shockwave exposure [28, 29]. Therefore, it is recommended clinically that contrast agents should not administrated prior to or during SWL. Doppler ultrasound can image flowing blood in major blood vessels but has difficulty in detecting static blood pool from hemorrhage of microvessels. Lacking a real-time imaging technique to monitor the vessel conditions in the clinics, urologists commonly have to push the SW dose to the upper limit in order to comminute stones in a short time. By doing so, patients are suffering from high risks of intra- and peri-renal vascular injury that can lead to acute and long-term adverse consequences [25]. Tapping the full potential of SWL, especially its noninvasiveness, relies on not only ongoing work to determine the mechanisms of tissue injury, but also new imaging methods for real-time monitoring of SWL-induced vascular injury.

Photoacoustic tomography (PAT) is promising to address this unmet clinical need. In PAT, excitation light is absorbed by tissue and converted into pressure waves via the photoacoustic effect, which are subsequently received by an ultrasonic transducer array to

form an image [30]. The laser illumination used in PAT has a typical surface optical fluence well below the ANSI safety limit [31]. PAT has been widely used in a variety of biomedical applications providing hemodynamic information such as vascular structure, oxygen saturation of hemoglobin [32], blood flow speed [33], and metabolic rate of oxygen [34]. PAT is thus promising for label-free imaging of the renal vasculature hemorrhage in SWL. Using hemoglobin as endogenous contrast, the changes in the blood flow and distribution due to shockwave-induced vascular injury, such as hemorrhage and onset of hematoma in deep renal tissues, may potentially be detected by PAT before severe adverse effects are produced during SWL [35].

Cavitation is a primary mechanism for vascular injury in SWL [29, 36]. Therefore, it is important to monitor the distribution of cavitation bubbles produced in SWL, assess their progression, and correlate their collapse with the resultant hemorrhage (*i.e.*, vessel rupture). Several optical and acoustic techniques have been used for cavitation detection, including high-speed photography in optically transparent media [15], as well as active cavitation detection (ACD) and passive cavitation detection (PCD) that can be applied to soft tissues [37]. ACD detects the ultrasound waves reflected by the bubbles in a transmission-receiving mode, and PCD detects cavitation collapse signals in a receiving-only mode. Compared to ACD, PCD does not affect cavitation activities. An ultrasonic transducer array is typically used to provide two-dimensional mapping of cavitation events, *i.e.*, passive cavitation mapping (PCM). PCM enables flexible detection of cavitation bubbles [38–40], and is compatible with PAT. Both PAT and PCM rely on receiving-only acoustic detection: while PAT detects signals generated by laser excitation, PCM detects signals generated by the collapse of cavitation bubbles.

In this work, we have integrated three technologies: SWL for fragmenting stones, PAT for monitoring the vascular injury during the treatment, and PCM for detecting the cavitation activity. We have developed a deep-penetrating PAT system based on a programmable ultrasound scanner, and integrated the PAT system with a clinical shockwave lithotripter. We have demonstrated the performance of the integrated system using phantoms, and its real-time label-free imaging of the vascular injury during SWL on a small animal model. Together with our recently developed internal light illumination strategy that can potentially provide deep penetration [41], we expect the integrated system will allow urologists to adjust the SWL treatment in time to minimize the risk of extensive tissue damage (*e.g.*, hematoma formation).

II. Methods

A. The integrated SWL/PAT/PCM system

Figure 1(a) shows the schematic of the integrated system, which includes three subsystems: SWL, PAT and PCM. In the SWL subsystem, a focused shockwave generator (Piezoson 100, Richard Wolf, Germany) transmits microsecond ultrasonic pulses, with a focal distance of 65 mm. The shockwave pulse is adjustable with a maximum in-focus pressure of ~60 MPa and a pulse repetition frequency (PRF) of 1 Hz. The PAT subsystem includes a 128-channel programmable ultrasound scanner (Vantage 128, Verasonics, USA) and a linear ultrasonic transducer probe (L7–4, Philips, USA; Central frequency: 5 MHz). The excitation light

source for PAT is a Q-switched Nd:YAG laser (Q-smart 850, Quantel Laser, USA; Wavelength: 1064 nm). The emitted light pulse is coupled into a bifurcated line optical guide (53–987, Edmund Optics, USA). The ultrasound probe is flanked by the two outputs of the light guide along the lateral sides. The two light beams intersect at the elevational focus of the ultrasound probe, which is 25 mm beneath the surface of the probe. The PCM subsystem shares the same ultrasonic detection with the PAT. A high-speed CMOS camera (Phantom 7.3, Vision Research, USA) is used to validate the PCM results in water.

We precisely synchronize the shockwave transmission, PCM signal acquisition, laser firing, and PAT signal acquisition. The trigger signals are sent by a lab-made control box, as illustrated in Fig. 1(b). The shockwave generator is triggered at 1 Hz, which also initiates the PCM and PAT data acquisition sequences. There is a 60-μs delay time from the trigger of shockwave generator to begin the PCM signal acquisition, ensuring all the possible cavitation events induced by the incident shockwave can be captured. There is a 500-ms delay between the shockwave transmission and the laser firing to avoid the overlapping between the cavitation signals and PA signals. To minimize the system's jitter, the laser's Q-switch is synchronized with the PA signal acquisition. Using our current laser, PAT can achieve a frame rate up to 10 Hz. We use a PA frame rate of 1 Hz in this study to reduce the total data size for longitudinal monitoring.

We use a delay-and-sum (DAS) based method for the PCM image reconstruction [42] and an iterative total-variation (TV) based method for the PAT image reconstruction [43, 44]. The TV-norm regularization is a widely used strategy in model-based PAT image reconstruction. It uses TV-norm of the absorbed energy density as the regularization term (or penalty term) of the objective function in the reconstruction. The TV-norm is effective for removing the high frequency noise without affecting the boundaries. The DAS-based method is faster than the TV-based method, and thus is preferred in PCM to reduce the processing time on a large amount of cavitation data [42]. Meanwhile, the TV-based method produces fewer high-frequency artifacts than the DAS-based method, and thus TV-based method is preferred in PAT to improve the image quality of small hemorrhages [43, 44].

In PCM, the DAS-based reconstructed image size is 40 mm (laterally) by 50 mm (axially) with a pixel size of 65 μm. A bandpass filter (cutoff frequencies: 3.5 MHz and 6.5 MHz), which corresponds to the bandwidth of the ultrasonic transducer array, is applied to the raw channel data before the image reconstruction. The speed of sound used is 1540 m/s. Each DAS reconstruction takes ~5 seconds. In PAT, the TV-based reconstructed image size is 60 mm (laterally) by 35 mm (axially) with a pixel size of 100 μm. The same bandpass filter is used as in PCM. The average number of iterations is 50. Each TV reconstruction takes ~18 seconds.

B. Characterization of PAT on phantoms

We first quantified PAT's spatial resolutions by imaging a black hair with a diameter of ~100 μm immersed in water as a line source (Fig. 2(a)). The distance between the hair and the probe surface was ~25 mm. The full-width-at-half-maximum of the hair profile in the reconstructed PA image was measured as the spatial resolution. We then measured PAT's maximum penetration depth by imaging a 2-mm-diameter plastic tube filled with whole

bovine blood (Quad Five, MT, USA). The tube was embedded at different depths in an optically scattering medium made of gelation and 0.5% whole milk. The estimated reduced optical scattering coefficient is ~6 cm^{-1} at 1064 nm [45, 46]. A total of 300 frames were averaged at each depth. The signal to noise ratio (SNR) was quantified as a function of depth. After characterizing PAT's key imaging performance, we also demonstrated 3D imaging of a mouse *in vivo*.

C. PCM of shockwave-induced cavitation

Passive cavitation mapping was initially introduced for studying high intensity focused ultrasound (HIFU) treatment. HIFU treatment typically utilizes longer and faster pulses than SWL, and the HIFU-induced cavitation events are often tightly confined in space and in time [47, 48]. By contrast, in SWL, the shockwave focus is much larger (up to a few centimeters axially), and the pulse is slower (1~10Hz), resulting in a less confined cavitation distribution in space and in time after each shockwave pulse.

Here, we have developed a sliding-window-based PCM method to reconstruct the spatial and temporal distribution of shockwave-induced cavitation events. It is crucial for PCM to find the correct time origin of the cavitation bubble collapse to reconstruct the correct location of the event. In our PCM experiments, the collapsed bubbles can be approximated as sparsely distributed point sources. A correct time origin leads to a point-shaped pattern in the PCM reconstruction, while an incorrect time origin generates a converging or diverging pattern. In other words, as the time origin is approaching the optimized value, the reconstructed bubble is converging into a point in space. Therefore, we have developed a sliding-window algorithm to search for the optimized time origin for each cavitation event. The signal amplitude in the reconstructed PCM image can be written as [49]:

$$H\left(\vec{r}\right) = \sum_{l=1}^{L} a\left(\vec{r_l} - \vec{r}\right) * p_l\left(\tau + \frac{\left|\vec{r_l} - \vec{r}\right|}{c}\right) \quad (1)$$

Here, $H\left(\vec{r}\right)$ is the reconstructed signal amplitude at location $\vec{r}$, a denotes the ultrasound probe's angular detection sensitivity, l is the index of the ultrasound probe element, $\vec{r_l}$ is the location of the lth probe element, p_l is the signal recorded by the lth element, τ is the starting time of the sliding window (*i.e.*, the time origin to be optimized), and c is the speed of sound. In our experiments, we used a 30-μs window for each reconstruction instance, and then slid the window by 2 μs for the next reconstruction instance. A representative sliding-window PCM reconstruction process is shown in Supplementary Video 1 (Videos can be found under the "Supplementary Files" tab in ScholarOne Manuscripts).

D. Validation of PCM in clear medium using a high-speed camera

Laser-induced single-bubble cavitation was performed to demonstrate the feasibility of our sliding-window PCM reconstruction method. The experimental setup is shown in Fig. 3(a). The pulsed laser beam at 532 nm was expanded and then focused by a convex lens into a water tank. A single bubble was produced when the laser pulse energy reached the optical breakdown threshold [50]. A high-speed CMOS camera captured the laser-induced bubble

through an optical window of the water tank. The ultrasound probe was placed 3 cm above the laser focus and the high-speed CMOS camera's imaging plane was aligned with the ultrasound probe's imaging plane. The laser firing was synchronized with the PCM detection and high-speed camera imaging. The camera's frame rate was 100 kHz, and PCM's sampling rate (or frame rate) was ~20 MHz. The sliding-window PCM method was used to reconstruct 2D mapping of the bubble collapse events. To better visualize cavitation bubble events, all the reconstructed instances with different time origins were stacked into a 3D data volume, from which we traced the cavitation's space origin based on the signal's converging pattern (Methods, Section C). The time tracing scheme is illustrated in Supplementary Fig. 1 (Figure can be found under the "Supplementary Files" tab in ScholarOne Manuscripts).

In addition to laser-induced single bubble, the behavior of a group of bubbles induced by shockwaves was also investigated, as shown in Fig. 4(a). The water tank with the shockwave generator installed at the bottom was filled with degassed water. The ultrasound probe's imaging plane was aligned orthogonally to the shockwave propagation direction in order to avoid signal overlapping. The focal distance of the shockwave generator is 65 mm, and the ultrasonic transducer probe was placed ~45 mm away from the shockwave focus. Based on this geometry, the earliest possible cavitation signals should arrive at the ultrasonic transducer at least ~71 μs after the shockwave emission, assuming a speed of sound of 1540 m/s in water and soft tissues. Therefore, the 60-μs delay before the PCM signal acquisition ensured that the highest number of cavitation events were imaged. The data acquisition duration for each shockwave pulse was 340 μs. Cavitation events induced by 100 shockwave pulses were recorded. A high-speed camera captured the cavitation events to validate the PCM results.

To further validate the PCM method, the effect of shockwave intensities on the cavitation generation was investigated, in which five shockwave levels of 4, 8, 12, 16, and 20 were used. At each shockwave level, 30 shockwave pulses were recorded with a 500-μs record duration for each pulse. The PCM results were validated by the high-speed camera images. The results are shown in Supplementary Fig. 2 (Figure can be found under the "Supplementary Files" tab in ScholarOne Manuscripts).

E. Simultaneous PAT of tissue injury and PCM of cavitation in vivo

We demonstrated simultaneous PAT and PCM during SWL treatment *in vivo* on healthy Swiss Webster mice (female; 10 weeks old; ~30 grams in weight). The protocol was approved by the Institutional Animal Care and Use Committee of Duke University. The hairs on the mouse's back and abdomen were removed. The experimental setup is shown in Fig. 6(a). The mouse was anesthetized with isoflurane (1.0 v/v flow rate). The water tank was filled with degassed water for shockwave coupling. The shockwave focus was positioned around the back muscle of the mouse. The imaging plane of the PAT and PCM was aligned with the shockwave generator's acoustic axis. Laser pulses at 1064 nm (pulse energy: ~30 mJ) were delivered to the skin surface. A baseline PAT image was acquired before applying the shockwaves. A total of 1000 shockwave pulses were applied at an energy level of 15. For each shockwave pulse, we reconstructed one PAT image and one PCM image. All the other

experimental settings were the same as the phantom experiments. To further test the integrated SWL-PAT-PCM system on detecting different levels of hemorrhage, we performed four more animal experiments at shockwave energy levels of 0, 6, 12 and 18, respectively. We targeted the vasculature around the liver with rich blood perfusion. A total of 600 shockwave pulses were applied on each animal.

III. Results and discussion

A. Characterization of the PAT and PCM system

The performance, including the imaging resolution and imaging depth, of the integrated system was evaluated first. The PAT's lateral and axial resolution at the elevational focus (25 mm from the probe surface) are 400 μm and 425 μm, respectively (Fig. 2(b-c)), consistent with our previous work [41]. We measured the maximum penetration depth of PAT at 1064 nm in optically scattering medium (Fig. 2(d)). The tube was clearly imaged at depths up to 7 cm. The SNR decreased with imaging depth. The decay constant was ~5 dB/cm or 1.8 cm^{-1} (Fig. 2(e)). Moreover, a 3D image of the mouse was acquired by scanning the ultrasonic probe along the elevational direction for 3.5 cm. A 3D focal-line reconstruction method was used to reconstruct the 3D image [51, 52]. A maximum amplitude PAT image projected along the axial dimension was superimposed on the ultrasound projection image (Fig. 2(f)). The volumetric rendering of the 3D PA image is shown in Fig. 2 (g).

To validate the feasibility and accuracy of the PCM method, we performed single-bubble and group-bubble studies, and compared the PCM results with the images from the high-speed camera. In the single-bubble PCM experiment, we clearly observed the initial cavitation collapse at 96 μs after the laser firing (Fig. 3(b)). We confirmed from the high-speed camera imaging that the bubble collapse time was indeed between 90 μs to 100 μs after the laser firing, as the camera had a temporal resolution of 10 μs (Fig. 3(c)). A secondary bubble collapse at 142 μs was also captured by PCM, which was induced by the collapse of the initial bubble (Fig. 3(d)). The secondary bubble collapse was again confirmed by the camera results (Fig. 3(e)). Therefore, the PCM results agree well with the high-speed camera results, and PCM can provide more accurate bubble collapse time. The dynamics of the single bubble generation and collapse are shown in Supplementary Video 2. Our sliding-window PCM method also generated a cavitation time trace that helped find the cavitation's spatial center. Figure 3(f) shows two representative bowtie-shaped time trace patterns for two bubble collapse events. The center of the bowtie pattern (or the most converged point) indicates that the sliding-window has reached the correct bubble collapse time. The two "wings" of the bowtie-pattern indicate the conditions that the sliding-window are either before or after the correct collapse time.

In the group-bubble study, the high-speed camera was used to record bubbles induced by a single shockwave pulse. Figure 4(b) is a representative camera image acquired at 70 μs after the shockwave pulse transmission, in which the dark features are the bubbles with diameters up to 0.7 mm. The PCM reconstruction at 140 μs after the shockwave pulse transmission is shown in Fig. 4(c). The cavitation collapse detected by PCM corresponds to the centers of the bowtie-shaped patterns in the PCM images. We used a Matlab's built-in circle-finding function to search for the bowtie-pattern centers, as shown by the blue circles in Fig. 4(c).

The retrieved cavitation centers were then assembled in Fig. 4(d), which shows three bubble collapse events at this moment. It is worth pointing out that the results from PCM and the camera do not represent exactly the same cavitation events, simply because the two modalities have different field of views, temporal resolutions, and contrast mechanisms (high-speed camera captures existing bubbles while PCM captures collapsing bubbles). For each shockwave pulse, by overlaying all the PCM instances, we can show the cavitation traces in the imaging plane (Fig. 4(e)). The brightness of Fig. 4(e) represents the frequency of cavitation events. By searching through all the PCM reconstruction instances, the distribution of cavitation events could be mapped in space (Fig. 4(f)). Representative time traces of group bubbles from one shockwave pulse are shown in Fig. 4(g).

We recorded 100 shockwave pulses and mapped their cavitation events. We quantified the number of cavitation events in the entire field of view as a function of time after each shockwave pulse. Each column in Fig. 5(a) represents the normalized probability of cavitation events induced by one shockwave pulse. The same process was performed on the camera images of 10 shockwave pulses (Fig. 5(b)). Figures 5(a)-(b) show a highly consistent cavitation pattern after each shockwave pulse: the first group of cavitation bubbles collapsed at ~110 μs, and the second group of cavitation bubbles collapsed at ~240 μs. Figures 5(c-d) are the averaged cavitation distribution obtained by PCM and the camera, respectively, also showing two groups of cavitation events. The second group of cavitation events might be induced by the residual shockwaves first reflected by the water surface on the top and then refocused by the shockwave generator surface at the bottom. There is a time delay between the high-speed camera results and the PCM results, because the camera detects existing bubbles while PCM detects the bubble collapses.

PCM was also performed in water at different shockwave pulse energy levels, and the results are shown in Supplementary Fig. 2 (Figure can be found under the “Supplementary Files” tab in ScholarOne Manuscripts). Supplementary Fig. 2(a) shows the PCM-detected cavitation collapse after each shockwave pulse, from 30 shockwave pulses in total. Firstly, regardless of the shockwave energy settings, we found that the earliest cavitation signals arrived at similar times after the shockwave emission, which was confirmed by the high-speed camera images (Supplementary Fig. 2(b)). Secondly, the total number and duration of the cavitation activities increased with the shockwave energy levels, because a higher SW energy leads to more and bigger bubbles that last longer. The average cavitation distribution obtained by PCM and the high-speed camera are shown in Supplementary Figs. 2 (c)-(d). Similar trends were found using these two imaging modalities.

From the above three studies on cavitation generated by SWL, we observed high consistency between the results from PCM and high-speed cameras, which demonstrated the feasibility of using PCM to detect cavitation activities. However, unlike the high-speed camera, PCM is not restricted to clear medium and can be easily applied for *in vivo* cavitation detection.

B. Simultaneous in vivo PAT and PCM

For *in vivo* experiments on mice, we simultaneously acquired B-mode ultrasound images (Fig. 6(b)), PAT images, and PCM images of the tissue region treated by shockwaves. Figure 6(c) shows representative PAT images before and after applying up to 1000 shockwave

pulses. Substantial PA signal increase due to hemorrhage was observed in the shockwave focus. The hemorrhage dynamics can be captured by PAT with a cross-sectional frame rate of 1 Hz. As shown in Fig. 7(a), two major blood vessels, marked as vessel #1 and #2, were monitored. Hemorrhage was observed close to vessel #1 after 40 shockwave pulses. After 70 shockwave pulses, the hemorrhage grew larger and the damaged vessel #1 shrank. The diameter of the vessel #2 also decreased without obvious hemorrhage observed, probably because the two blood vessels were connected. The hemorrhage dynamics detected by PAT are shown in Supplementary Video 3. Changes in the average PA signal amplitude within the hemorrhage region were quantified, as shown in Fig. 7(b). The PA signals increased gradually up to shockwave pulse #400, slightly decreased from pulse #400 to #500, and then increased sharply at pulse #530, reflecting the multiple phases of shockwave-induced vascular injury, including hemorrhages, blood pool formation, and diffusion into the surrounding tissues. After 700 shockwave pulses, the PA signals were stable, indicating the hemorrhage was over.

The cavitation events induced by shockwave pulses were also recorded by PCM with a frame rate of 1 Hz. Figure 8(a) shows one representative PCM reconstruction instance of cavitation signals at 116 μs after shockwave pulse #520. We can observe multiple cavitation events within the shockwave focus. Yet it was clear that the *in vivo* PCM images have more artifacts, which is mostly due to the acoustic scattering and reverberation in the tissue. By assembling all the cavitation events (Figs. 8(b-c)), we observed that these events were largely distributed along the shockwave propagation path and around the shockwave focus. We overlapped the PCM images with the PAT images (Fig. 8(d)), and it is clear that the cavitation regions were consistent with the hemorrhage sites.

We also performed animal experiments at different SW energy settings (Fig. 9). Without shockwave treatment, no clear changes in the PA signals were observed. With increased shockwave pulse energy, we observed elevated hemorrhages at various time points during the treatment. In addition, more hemorrhage regions were observed at higher shockwave energy levels. We also reconstructed the cavitation events at different shockwave energy levels, as shown in Fig. 10(a). The results confirmed that more cavitation events within larger regions were generated at higher shockwave energy levels, which matched well with the PAT results (Fig. 10(b)).

IV. Conclusion

In this work, we have developed an integrated SWL-PAT-PCM system that is capable of simultaneously monitoring the shockwave-induced vascular injury, as well as the cavitation events that are mostly responsible for the damage. Three subsystems were seamlessly integrated with balanced spatial resolution and penetration depth. Compared with existing imaging modalities in SWL, such as X-ray fluoroscopy and ultrasound imaging, PAT is superior because it is non-ionizing, non-invasive, and more sensitive to blood. The sliding-window PCM reconstruction was validated by using a high-speed CMOS camera. *In vivo* mouse imaging has further demonstrated that tissue damage by shockwave treatment can be monitored by PAT, together with simultaneous cavitation mapping by PCM. These results

have collectively proved that the integrated system has a high potential for predicting and monitoring hemorrhage during SWL treatment.

The major concern of the current PAT system is the limited penetration depth. Averaged over all stone patients, the skin surface is ~10 cm from the posterior boundary of the kidney [53]. However, traditional PAT technologies are limited by optical attenuation to ~7 cm in soft tissue, due to both optical absorption and scattering [54]. Therefore, imaging the deeply seated human kidney will require extending the penetration depth of PAT to at least 10 cm. On one hand, previous studies by other groups have demonstrated that PAT, with external light illumination, can achieve a penetration depth of ~6–10 cm by using exogenous contrast agents that have strong optical absorption at 1064 nm [55]. However, using exogenous contrast agents on patients may meet significant safety and regulatory hurdles, and thus is not preferred. On the other hand, our recent study has achieved a 7-cm imaging depth in biological tissues by using internal light illumination and external ultrasound detection [41]. Based on this work, we believe that a promising solution is to illuminate the deep-seated kidney from the inside using a flexible and thin optical fiber inserted through the ureter, while the ultrasound signals can be detected outside on the skin surface.

Rodent models with mm-sized stone (not crystal) formation are not available despite many years of research, and it is challenging to surgically implant kidney stones in small animal models, limited by the small size of the mouse kidney. In the future work, we will apply our SWL-PAT-PCM system on large animal models with implanted kidney stones [56], to demonstrate simultaneous stone comminution, cavitation detection, and hemorrhage monitoring. Ultimately, we expect that our non-invasive, non-ionizing SWL-PAT-PCM system will be applied to optimize the safety and efficiency of SWL treatment in clinics. In fact, many clinical lithotripters (*e.g.*, Siemens LITHOSKOP and STORZ Modolith SLX) already have a central port in the shockwave generator for incorporating an ultrasound probe, which can be used for PAT/PCM imaging [57]. Alternatively, the PAT/PCM imaging probe can be mounted on an articulated arm, moving isocentrically around the shockwave focal point in order to search for the optimal imaging window.

Supplementary Material

Refer to Web version on PubMed Central for supplementary material.

Acknowledgments

This work was supported by Duke MEDx fund, Duke GCB faculty award, AHA collaborative sciences grant 18CSA34080277, NIH grant R01EB028143, R01 NS111039, and R21 EB027304 (all to J.Y.) and R37-DK052985–22 (to P.Z.). We thank Tri Vu and Yuqi Tang for editing the manuscript.

References

[1]. Pearle MS, Calhoun EA, Curhan GC, and Urologic P Diseases of America, “Urologic diseases in America project: urolithiasis,” J Urol, vol. 173, no. 3, pp. 848–57, 3, 2005. [PubMed: 15711292]

[2]. Scales CD Jr., Curtis LH, Norris RD, Springhart WP, Sur RL, Schulman KA, and Preminger GM, “Changing gender prevalence of stone disease,” J Urol, vol. 177, no. 3, pp. 979–82, 3, 2007. [PubMed: 17296391]

[3]. Stamatelou KK, Francis ME, Jones CA, Nyberg LM, and Curhan GC, “Time trends in reported prevalence of kidney stones in the United States: 1976–1994,” Kidney Int, vol. 63, no. 5, pp. 1817–23, 5, 2003. [PubMed: 12675858]

[4]. Taylor EN, Stampfer MJ, and Curhan GC, “Obesity, weight gain, and the risk of kidney stones,” JAMA, vol. 293, no. 4, pp. 455–62, 1 26, 2005. [PubMed: 15671430]

[5]. Mortality GBD, and Causes of Death C, “Global, regional, and national life expectancy, all-cause mortality, and cause-specific mortality for 249 causes of death, 1980–2015: a systematic analysis for the Global Burden of Disease Study 2015,” Lancet, vol. 388, no. 10053, pp. 1459–1544, 10 8, 2016. [PubMed: 27733281]

[6]. Litwin MS, and Saigal CS, “Introduction,” Urologic Diseases in America, Litwin MS and Saigal CS, eds., pp. 1–8, Washington, DC: US Department of Health and Human Services, Public Health Service, National Institutes of Health, National Institute of Diabetes and Digestive and Kidney Diseases, 2007.

[7]. Pearle MS, Lingeman JE, Leveillee R, Kuo R, Preminger GM, Nadler RB, Macaluso J, Monga M, Kumar U, Dushinski J, Albala DM, Wolf JS Jr., Assimos D, Fabrizio M, Munch LC, Nakada SY, Auge B, Honey J, Ogan K, Pattaras J, McDougall EM, Averch TD, Turk T, Pietrow P, and Watkins S, “Prospective, randomized trial comparing shock wave lithotripsy and ureteroscopy for lower pole caliceal calculi 1 cm or less,” J Urol, vol. 173, no. 6, pp. 2005–9, 6, 2005. [PubMed: 15879805]

[8]. Preminger GM, Tiselius HG, Assimos DG, Alken P, Buck C, Gallucci M, Knoll T, Lingeman JE, Nakada SY, Pearle MS, Sarica K, Turk C, Wolf JS Jr., and Panel EANG, “2007 guideline for the management of ureteral calculi,” J Urol, vol. 178, no. 6, pp. 2418–34, 12, 2007. [PubMed: 17993340]

[9]. Lotan Y, Cadeddu JA, Roehrborn CG, and Stage KH, “The value of your time: evaluation of effects of changes in medicare reimbursement rates on the practice of urology,” J Urol, vol. 172, no. 5 Pt 1, pp. 1958–62, 11, 2004. [PubMed: 15540765]

[10]. Xi X, and Zhong P, “Dynamic photoelastic study of the transient stress field in solids during shock wave lithotripsy,” J Acoust Soc Am, vol. 109, no. 3, pp. 1226–39, 3, 2001. [PubMed: 11303936]

[11]. Eisenmenger W, “The mechanisms of stone fragmentation in ESWL,” Ultrasound Med Biol, vol. 27, no. 5, pp. 683–93, 5, 2001. [PubMed: 11397533]

[12]. Zhu S, Cocks FH, Preminger GM, and Zhong P, “The role of stress waves and cavitation in stone comminution in shock wave lithotripsy,” Ultrasound Med Biol, vol. 28, no. 5, pp. 661–71, 5, 2002. [PubMed: 12079703]

[13]. Pishchalnikov YA, Sapozhnikov OA, Bailey MR, Williams JC Jr., Cleveland RO, Colonius T, Crum LA, Evan AP, and McAteer JA, “Cavitation bubble cluster activity in the breakage of kidney stones by lithotripter shockwaves,” J Endourol, vol. 17, no. 7, pp. 435–46, 9, 2003. [PubMed: 14565872]

[14]. Zhong P, Zhou Y, and Zhu S, “Dynamics of bubble oscillation in constrained media and mechanisms of vessel rupture in SWL,” Ultrasound Med Biol, vol. 27, no. 1, pp. 119–34, 1, 2001. [PubMed: 11295278]

[15]. Sankin GN, Simmons WN, Zhu SL, and Zhong P, “Shock wave interaction with laser-generated single bubbles,” Phys Rev Lett, vol. 95, no. 3, pp. 034501, 7 15, 2005. [PubMed: 16090745]

[16]. Zhong P, “Shock Wave Lithotripsy,” Bubble Dynamics and Shock Waves, Delale CF, ed., pp. 291–338, Berlin Heidelberg: Springer-Verlag, 2013.

[17]. Diaz-Tejeiro R, Garcia Diaz E, Fernandez G, Gonzalez E, Garcia MA, Ahijado F, Gomez E, Sierra T, and Iglesias A, “Irreversible acute renal failure after extracorporeal shock-wave lithotripsy,” Nephron, vol. 63, no. 2, pp. 242–3, 1993. [PubMed: 8450924]

[18]. Baskin LS, and Stoller ML, “Severe haemorrhage after extracorporeal shock wave lithotripsy: radiological evaluation,” Br J Urol, vol. 69, no. 2, pp. 214–5, 2, 1992. [PubMed: 1537039]

[19]. Silberstein J, Lakin CM, and Kellogg Parsons J, “Shock wave lithotripsy and renal hemorrhage,” Rev Urol, vol. 10, no. 3, pp. 236–41, Summer, 2008. [PubMed: 18836562]

[20]. Evan AP, and McAteer JA, “Q-Effects of shock wave lithotripsy,” Kidney Stones: Medical and Surgical Management, pp. 549–570, 1996.

[21]. Delius M, “Medical applications and bioeffects of extracorporeal shock waves,” Shock Waves, vol. 4, no. 2, pp. 55–72, 1994.

[22]. Willis LR, Evan AP, Connors BA, Handa RK, Blomgren PM, and Lingeman JE, “Prevention of lithotripsy-induced renal injury by pretreating kidneys with low-energy shock waves,” J Am Soc Nephrol, vol. 17, no. 3, pp. 663–73, 3, 2006. [PubMed: 16452495]

[23]. Evan AP, Willis LR, Lingeman JE, and McAteer JA, “Renal trauma and the risk of long-term complications in shock wave lithotripsy,” Nephron, vol. 78, no. 1, pp. 1–8, 1998. [PubMed: 9453396]

[24]. Willis LR, Evan AP, Connors BA, Blomgren P, Fineberg NS, and Lingeman JE, “Relationship between kidney size, renal injury, and renal impairment induced by shock wave lithotripsy,” Journal of the American Society of Nephrology, vol. 10, no. 8, pp. 1753–1762, 8, 1999. [PubMed: 10446943]

[25]. McAteer JA, and Evan AP, “The acute and long-term adverse effects of shock wave lithotripsy,” Semin Nephrol, vol. 28, no. 2, pp. 200–13, 3, 2008. [PubMed: 18359401]

[26]. Uemura K, Takahashi S, Shintani-Ishida K, Nakajima M, Saka K, and Yoshida KI, “A death due to perirenal hematoma complicating extracorporeal shockwave lithotripsy,” Journal of Forensic Sciences, vol. 53, no. 2, pp. 469–471, 3, 2008. [PubMed: 18366582]

[27]. Vaezy S, Andrew M, Kaczkowski P, and Crum L, “Image-guided acoustic therapy,” Annual Review of Biomedical Engineering, vol. 3, pp. 375–390, 2001.

[28]. Dalecki D, Raeman CH, Child SZ, Penney DP, Mayer R, and Carstensen EL, “The influence of contrast agents on hemorrhage produced by lithotripter fields,” Ultrasound Med Biol, vol. 23, no. 9, pp. 1435–9, 1997. [PubMed: 9428143]

[29]. Matlaga BR, McAteer JA, Connors BA, Handa RK, Evan AP, Williams JC, Lingeman JE, and Willis LR, “Potential for cavitation-mediated tissue damage in shockwave lithotripsy,” J Endourol, vol. 22, no. 1, pp. 121–6, 1, 2008. [PubMed: 18315482]

[30]. Wang LHV, and Yao JJ, “A practical guide to photoacoustic tomography in the life sciences,” Nature Methods, vol. 13, no. 8, pp. 627–638, 8, 2016. [PubMed: 27467726]

[31]. A. N. S. Institute, American national standard for safe use of lasers: Laser Institute of America, 2007.

[32]. Zhang HF, Maslov K, Stoica G, and Wang LHV, “Functional photoacoustic microscopy for high-resolution and noninvasive in vivo imaging,” Nature Biotechnology, vol. 24, no. 7, pp. 848–851, 7, 2006.

[33]. Fang H, Maslov K, and Wang LV, “Photoacoustic doppler effect from flowing small light-absorbing particles,” Physical Review Letters, vol. 99, no. 18, Nov 2, 2007.

[34]. Yao JJ, Maslov KI, Zhang Y, Xia YN, and Wang LV, “Label-free oxygen-metabolic photoacoustic microscopy in vivo,” Journal of Biomedical Optics, vol. 16, no. 7, 7, 2011.

[35]. Li M, Tang Y, and Yao J, “Photoacoustic tomography of blood oxygenation: A mini review,” Photoacoustics, vol. 10, pp. 65–73, 6, 2018. [PubMed: 29988848]

[36]. Carstensen EL, Gracewski S, and Dalecki D, “The search for cavitation in vivo,” Ultrasound Med Biol, vol. 26, no. 9, pp. 1377–85, 11, 2000. [PubMed: 11179611]

[37]. Madanshetty SI, Roy RA, and Apfel RE, “Acoustic microcavitation: its active and passive acoustic detection,” J Acoust Soc Am, vol. 90, no. 3, pp. 1515–26, 9, 1991. [PubMed: 1939908]

[38]. Norton SJ, and Won IJ, “Time exposure acoustics,” Ieee Transactions on Geoscience and Remote Sensing, vol. 38, no. 3, pp. 1337–1343, 5, 2000.

[39]. Norton SJ, and Linzer M, “Backprojection Reconstruction of Random Source Distributions,” Journal of the Acoustical Society of America, vol. 81, no. 4, pp. 977–985, 4, 1987.

[40]. Norton SJ, Carr BJ, and Witten AJ, “Passive imaging of underground acoustic sources,” Journal of the Acoustical Society of America, vol. 119, no. 5, pp. 2840–2847, 5, 2006.

[41]. Li M, Lan B, Liu W, Xia J, and Yao J, “Internal-illumination photoacoustic computed tomography,” J Biomed Opt, vol. 23, no. 3, pp. 1–4, 3, 2018.

[42]. Mozaffarzadeh M, Mahloojifar A, Orooji M, Kratkiewicz K, Adabi S, and Nasiriavanaki M, “Linear-array photoacoustic imaging using minimum variance-based delay multiply and sum adaptive beamforming algorithm,” Journal of Biomedical Optics, vol. 23, no. 2, 2, 2018.

[43]. Wang J, Zhang C, and Wang Y, "A photoacoustic imaging reconstruction method based on directional total variation with adaptive directivity," Biomed Eng Online, vol. 16, no. 1, pp. 64, 5 30, 2017. [PubMed: 28558769]

[44]. Hauptmann A, Lucka F, Betcke M, Huynh N, Adler J, Cox B, Beard P, Ourselin S, and Arridge S, "Model-Based Learning for Accelerated, Limited-View 3-D Photoacoustic Tomography," Ieee Transactions on Medical Imaging, vol. 37, no. 6, pp. 1382–1393, 6, 2018. [PubMed: 29870367]

[45]. Qin JW, and Lu RF, "Measurement of the absorption and scattering properties of turbid liquid foods using hyperspectral imaging," Applied Spectroscopy, vol. 61, no. 4, pp. 388–396, 4, 2007. [PubMed: 17456257]

[46]. Nikolakakos IP, Major A, Aitchison JS, and Smith PWE, "Broadband characterization of the nonlinear optical properties of common reference materials," Ieee Journal of Selected Topics in Quantum Electronics, vol. 10, no. 5, pp. 1164–1170, Sep-Oct, 2004.

[47]. Li T, Chen H, Khokhlova T, Wang YN, Kreider W, He X, and Hwang JH, "Passive cavitation detection during pulsed HIFU exposures of ex vivo tissues and in vivo mouse pancreatic tumors," Ultrasound Med Biol, vol. 40, no. 7, pp. 1523–34, 7, 2014. [PubMed: 24613635]

[48]. Gyongy M, Arora M, Noble JA, and Coussios CC, "Use of Passive Arrays for Characterization and Mapping of Cavitation Activity during HIFU Exposure," 2008 Ieee Ultrasonics Symposium, *Vols* 1–4 and Appendix, pp. 871–874, 2008.

[49]. Gyongy M, and Coussios CC, "Passive spatial mapping of inertial cavitation during HIFU exposure," IEEE Trans Biomed Eng, vol. 57, no. 1, pp. 48–56, 1, 2010. [PubMed: 19628450]

[50]. Akhatov I, Lindau O, Topolnikov A, Mettin R, Vakhitova N, and Lauterborn W, "Collapse and rebound of a laser-induced cavitation bubble," Physics of Fluids, vol. 13, no. 10, pp. 2805–2819, 10, 2001.

[51]. Xia J, Guo Z, Maslov K, Aguirre A, Zhu Q, Percival C, and Wang LV, "Three-dimensional photoacoustic tomography based on the focal-line concept," J Biomed Opt, vol. 16, no. 9, pp. 090505, 9, 2011. [PubMed: 21950908]

[52]. Wang D, Wang Y, Zhou Y, Lovell JF, and Xia J, "Coherent-weighted three-dimensional image reconstruction in linear-array-based photoacoustic tomography," Biomed Opt Express, vol. 7, no. 5, pp. 1957–65, 5 1, 2016. [PubMed: 27231634]

[53]. Bohris C, Bayer T, and Gumpinger R, "Ultrasound Monitoring of Kidney Stone Extracorporeal Shockwave Lithotripsy with an External Transducer: Does Fatty Tissue Cause Image Distortions That Affect Stone Comminution?," Journal of Endourology, vol. 24, no. 1, pp. 81–88, 1, 2010. [PubMed: 19961334]

[54]. Hai PF, Yao JJ, Li G, Li CY, and Wang LHV, "Photoacoustic elastography," Optics Letters, vol. 41, no. 4, pp. 725–728, 2 15, 2016. [PubMed: 26872173]

[55]. Zhou Y, Wang DP, Zhang YM, Chitgupi U, Geng JM, Wang YH, Zhang YZ, Cook TR, Xia J, and Lovell JF, "A Phosphorus Phthalocyanine Formulation with Intense Absorbance at 1000 nm for Deep Optical Imaging," Theranostics, vol. 6, no. 5, pp. 688–697, 2016. [PubMed: 27022416]

[56]. Neisius A, Smith NB, Sankin G, Kuntz NJ, Madden JF, Fovargue DE, Mitran S, Lipkin ME, Simmons WN, Preminger GM, and Zhong P, "Improving the lens design and performance of a contemporary electromagnetic shock wave lithotripter," Proceedings of the National Academy of Sciences of the United States of America, vol. 111, no. 13, pp. E1167–E1175, 4 1, 2014. [PubMed: 24639497]

[57]. Kim C, Erpelding TN, Jankovic L, Pashley MD, and Wang LHV, "Deeply penetrating in vivo photoacoustic imaging using a clinical ultrasound array system," Biomedical Optics Express, vol. 1, no. 1, pp. 278–284, 8 2, 2010. [PubMed: 21258465]

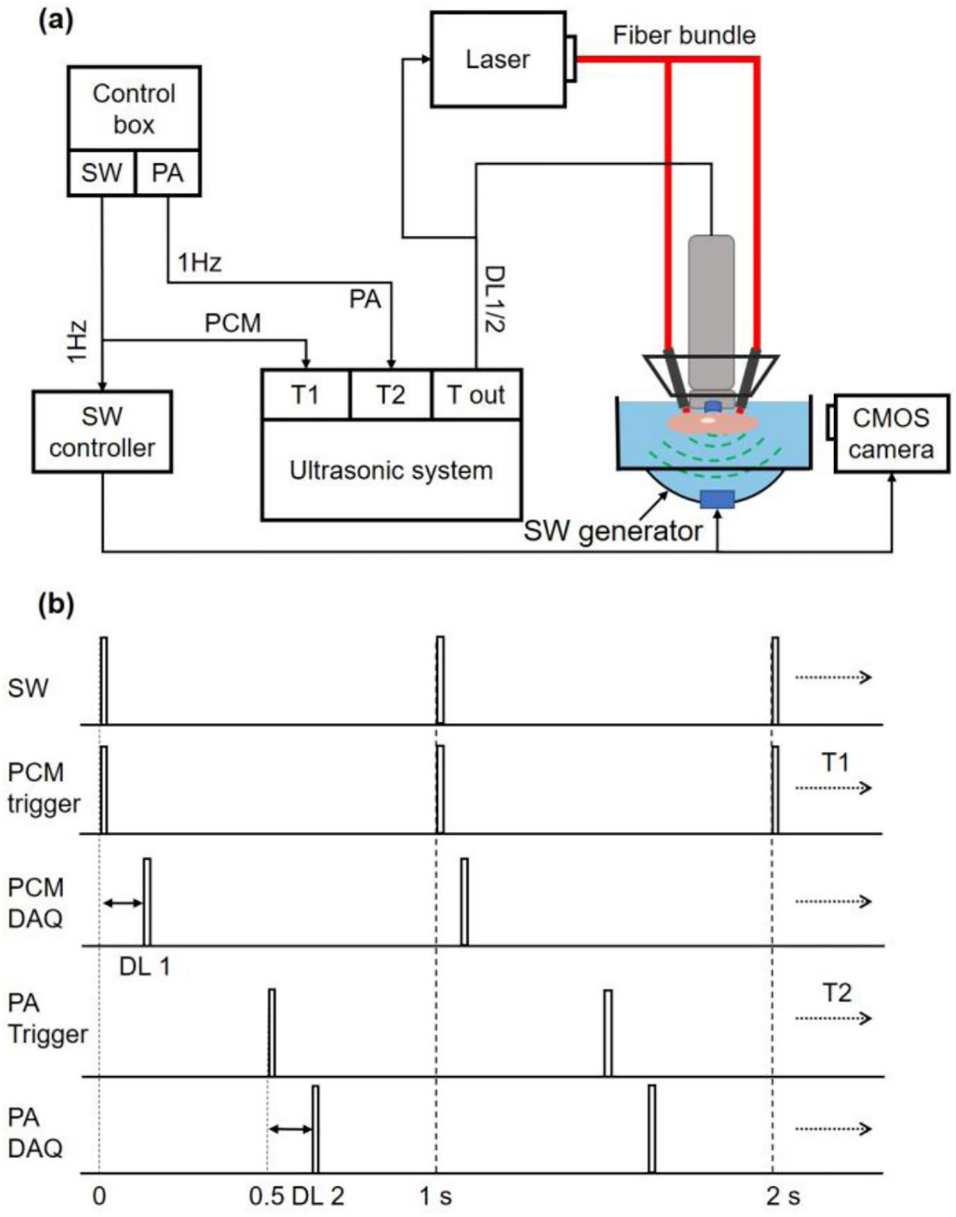

Fig. 1.

Integrating SWL/PAT/PCM into a single device. (a) Schematics of the SWL-PAT-PCM system. SW, trigger for shockwave transmission; PA, trigger for PA signal acquisition; T1, trigger-in port 1; T2, trigger-in port 2; T out, trigger-out; DL1, delay between shockwave transmission and PCM acquisition; DL2, delay between laser flashlamp trigger and PA signal acquisition/laser firing. (b) Time sequence of the triggers for shockwave transmission (SW), passive cavitation mapping (PCM DAQ) and PA imaging (PAT DAQ).

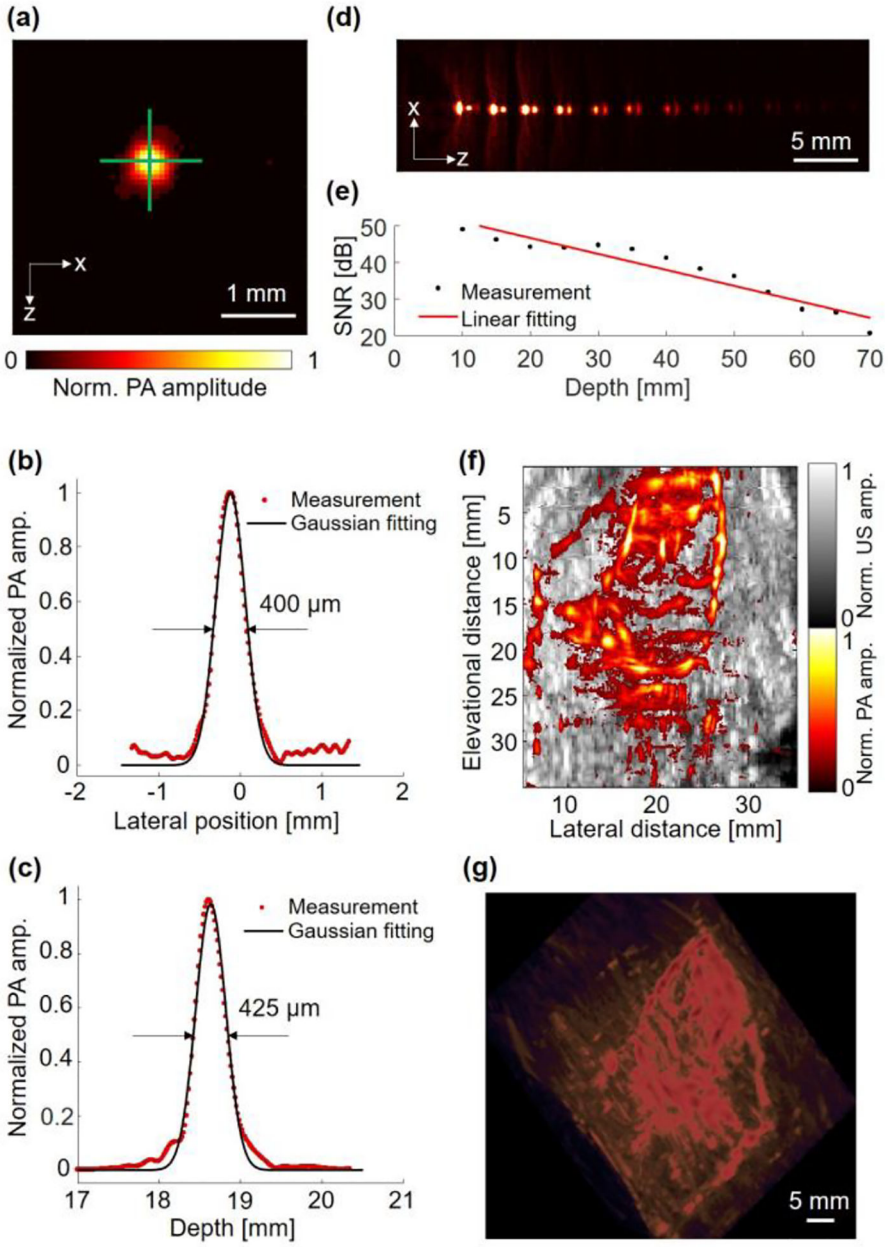

Fig. 2.

Characterization of the PAT system. (a) PAT image of a human hair at a depth of ~25 mm. (b) Lateral profile of the hair along the horizontal green line in (a). (c) Axial profile of the hair along the vertical green line in (a). (d) Composite PAT image of a plastic tube filled with whole bovine blood embedded at different depths in an optically scattering medium, acquired at 1064 nm. (e) Measured (black dotted line) SNR of the tube as a function of depth. A linear fitting (red solid line) quantified the signal attenuation coefficient. (f) Superimposed maximum amplitude projections of PA (shown in color) and US (shown in gray) image of the mouse trunk. (g) Volumetric rendering of the PA image of the mouse trunk.

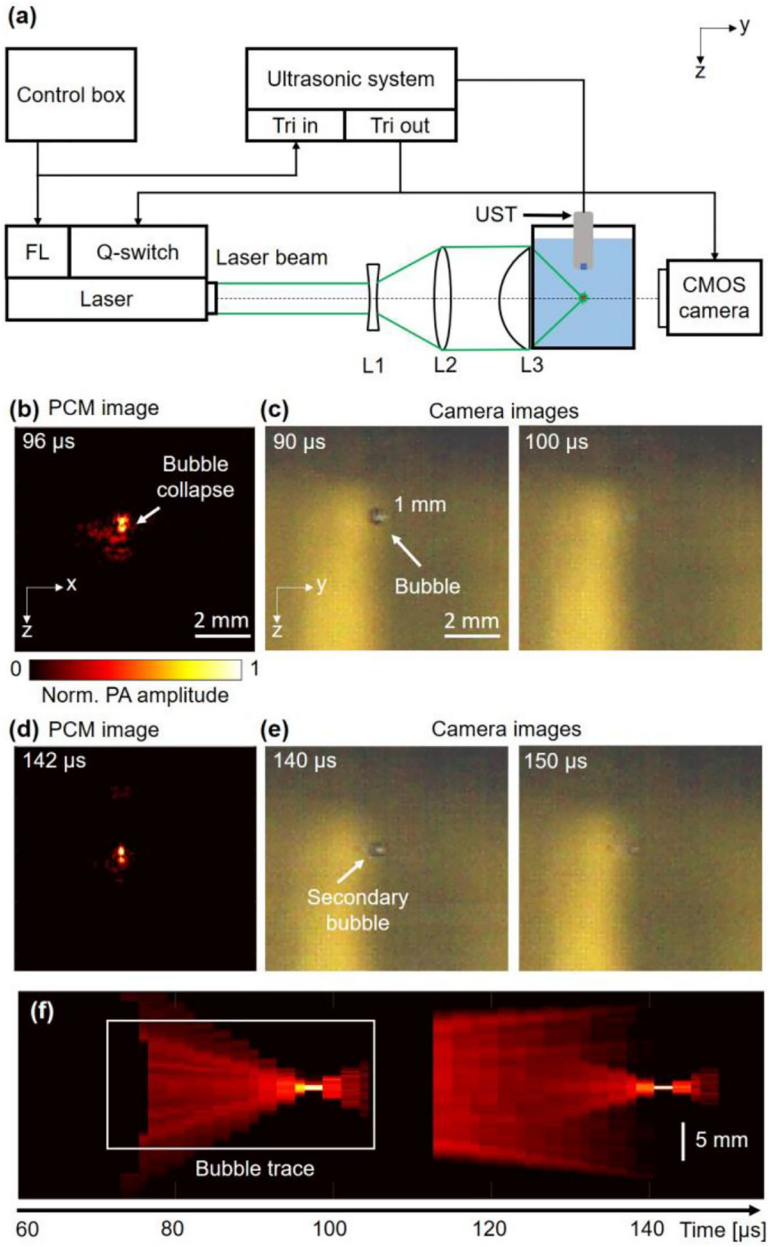

Fig. 3.

Laser-induced single-bubble cavitation detection using sliding-window PCM. (a) Schematic of cavitation detection experiment. (b) PCM image of the initial cavitation collapse at 96 µs after laser firing (Supplementary Video 1). (c) Photographs by high-speed camera at 90 µs and 100 µs after laser firing (Supplementary Video 2). (d) PCM image of the secondary cavitation collapse at 142µs after laser firing. (e) Photographs by high-speed camera at 140 µs and 150 µs after laser firing. (f) Representative single-bubble time traces by using PCM, showing the bowtie-shaped patterns (Supplementary Fig 1).

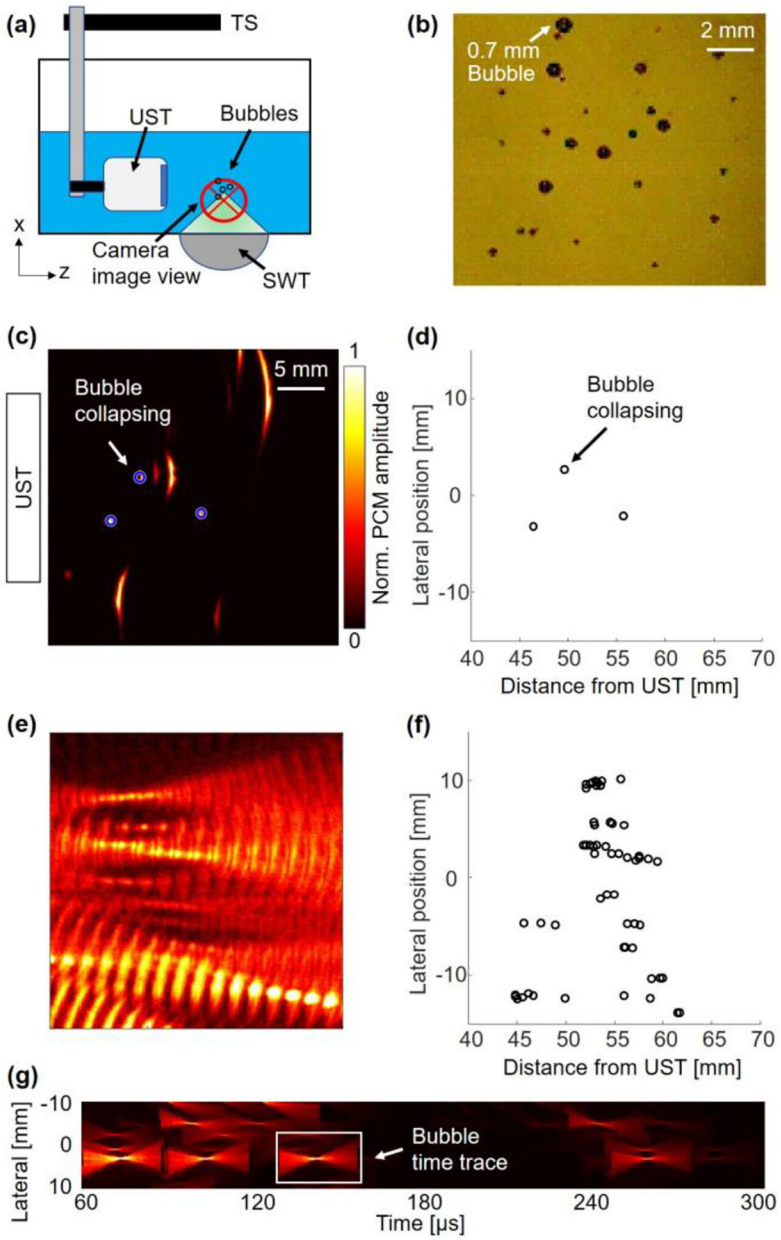

Fig. 4.

Shockwave-induced group-cavitation detection. (a) System setup of shockwave-induced cavitation detection, including high-speed camera imaging and sliding-window PCM. TS, translation stage; UST, ultrasonic transducer; SWT, shockwave transducer. (b) Photograph of group cavitation by high-speed camera at 70 μs after the shockwave firing. (c) One representative PCM reconstruction instance of cavitation signals at 140 μs. Three cavitation centers are labelled by blue circles. (d) Scatter plot of extracted cavitation centers obtained from (c). (e) Stacked PCM reconstruction instances with different sliding-windows over the same field of view. (f) Scatter plot of extracted cavitation centers induced by one shockwave pulse. (g) Representative group-bubble time traces induced by one shockwave pulse.

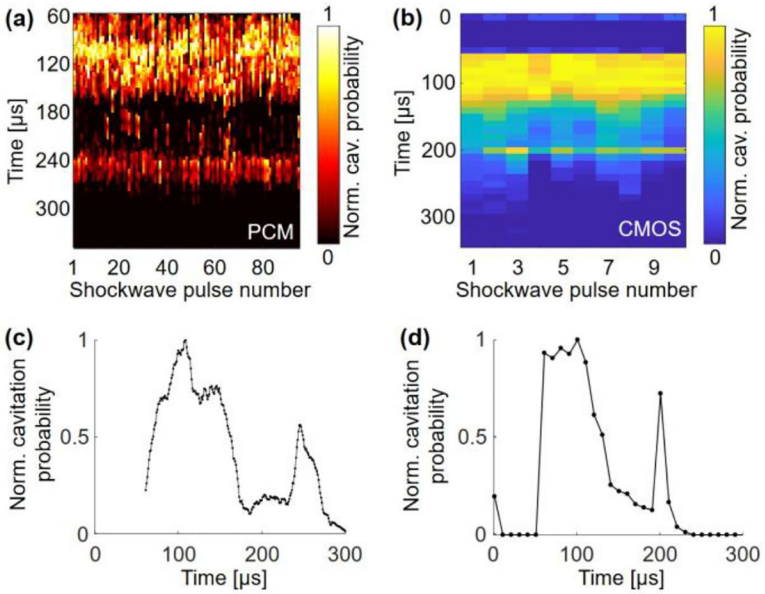

Fig. 5.

Cavitation analysis by PCM and the high-speed camera. (a) PCM-detected cavitation collapse probability after each shockwave pulse. A total of 100 shockwave pulses were analyzed. (b) Camera-detected cavitation probability after each shockwave pulse. A total of 10 shockwave pulses were analyzed. (c) Normalized cavitation collapse probability as a function of time, detected by PCM and averaged from the results of 100 shockwave pulses. (d) Normalized cavitation probability as a function of time, detected by the camera and averaged from the results of 10 shockwave pulses.

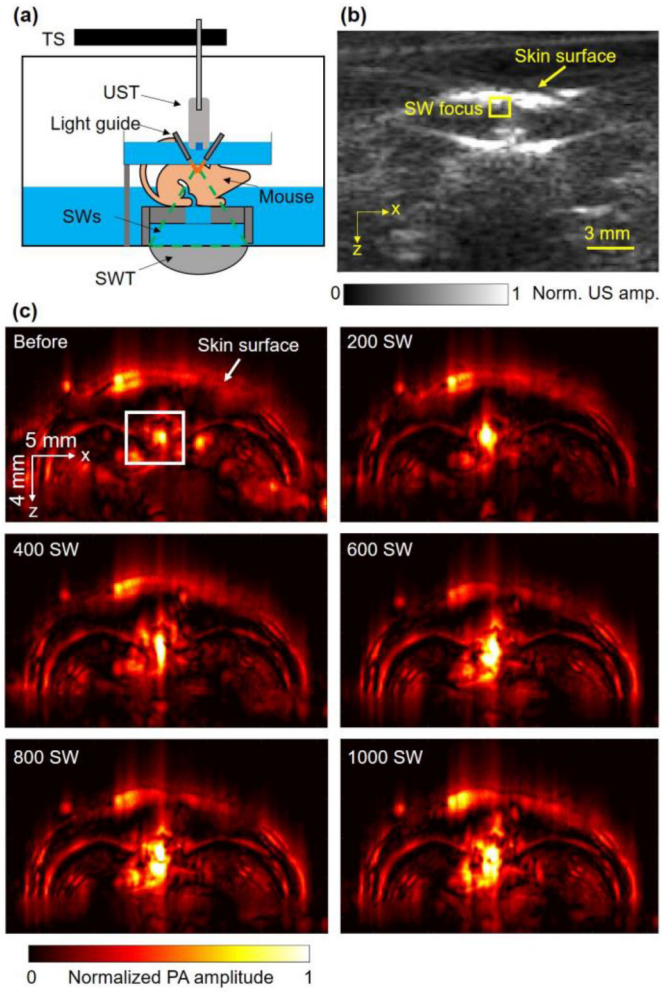

Fig. 6.

In vivo PAT of vascular injury induced by shockwave treatment. (a) Setup of the *in vivo* experiment. (b) B-mode ultrasound image of a mouse cross-section. The yellow rectangular represents the location of the shockwave focus. (c) PAT cross-sectional images of the mouse before and after 200, 400, 600, 800 and 1000 shockwave pulses.

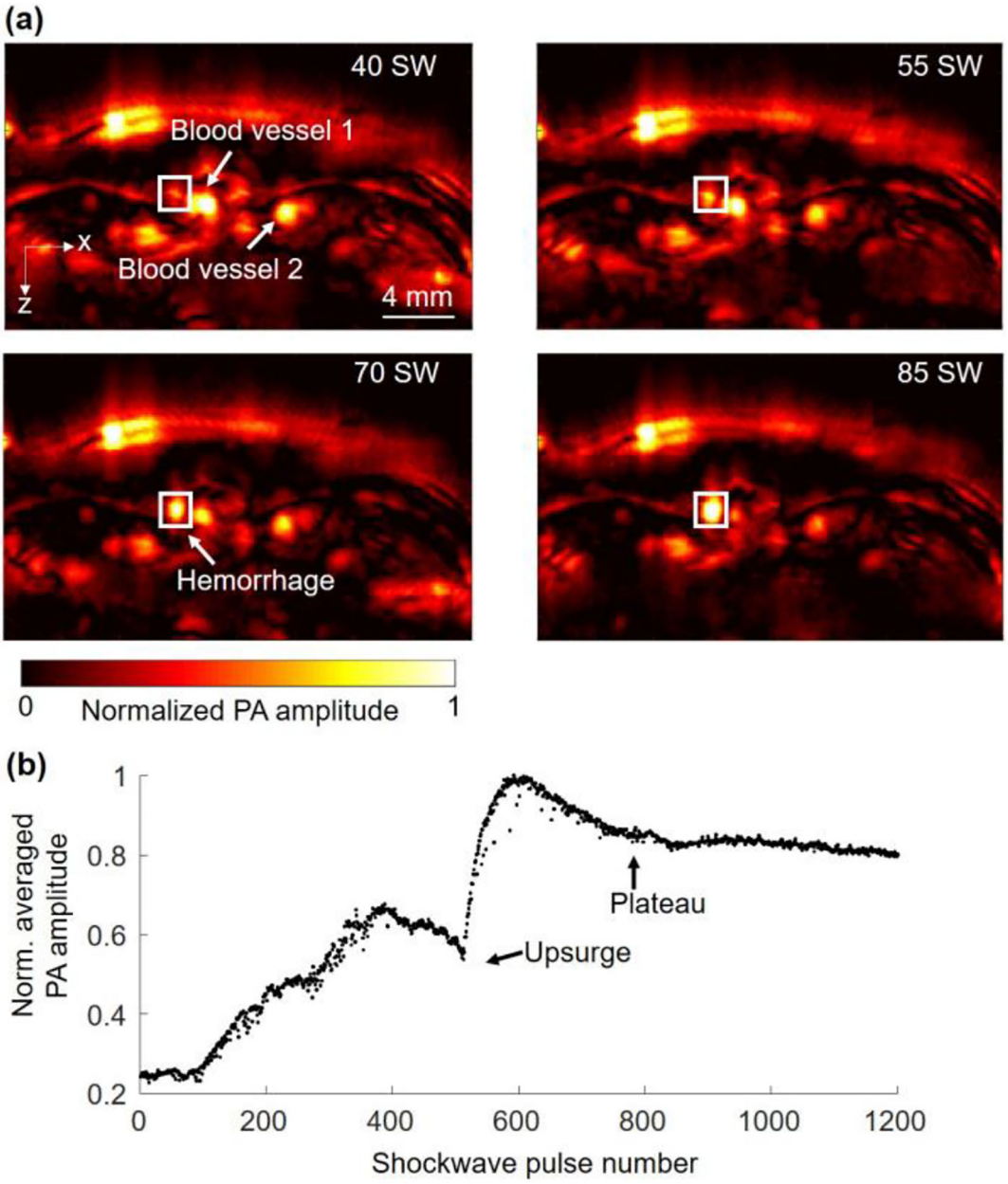

Fig. 7.

Representative hemorrhage dynamics monitored by PAT. (a) PAT images of the mouse cross-section after 40, 55, 70, and 85 shockwave pulses, respectively. The white rectangular regions indicate an enlarging blood pool (Video 3). (b) Time course of the relative change in the averaged PA signal amplitude within the rectangular regions in (a), showing the multiple phases of the vascular injury.

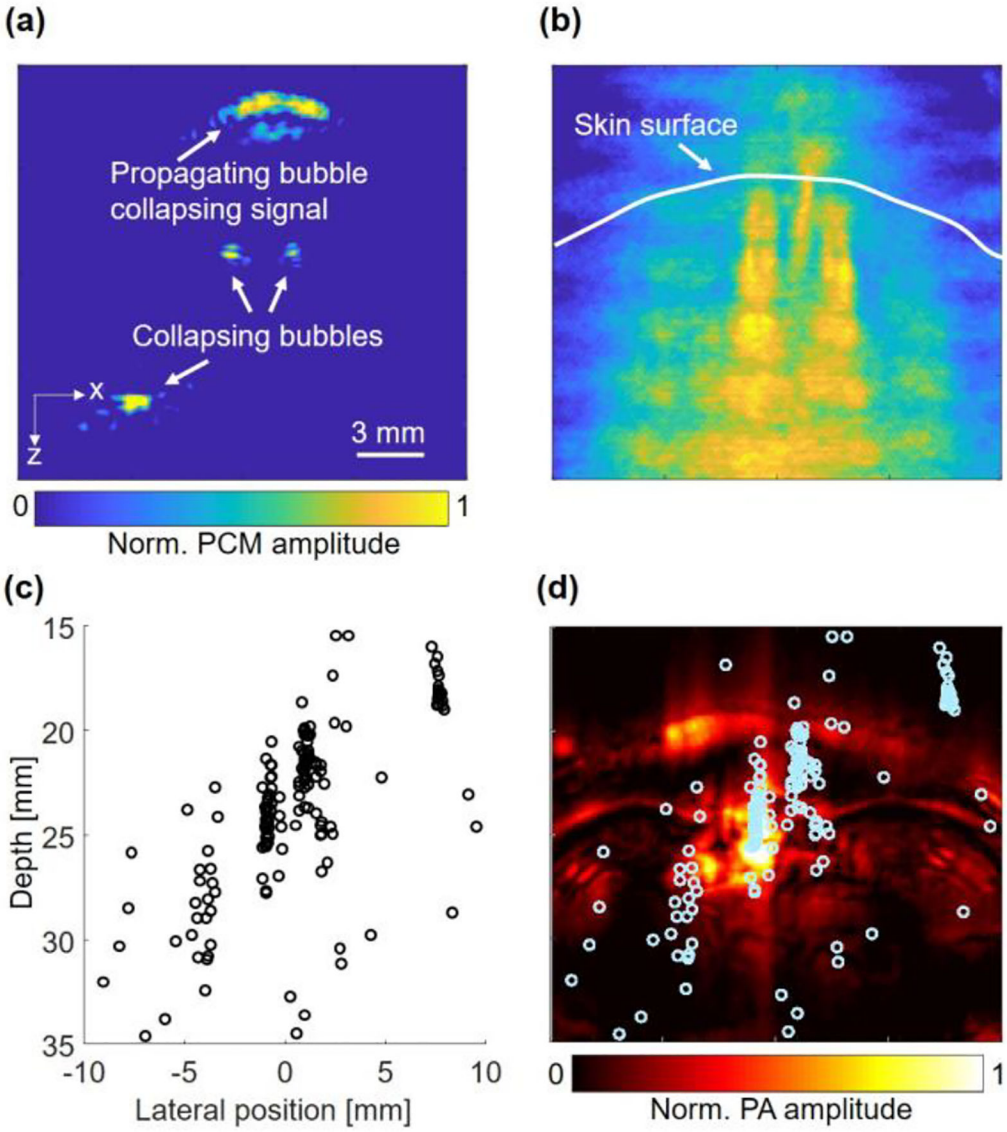

Fig 8.

In vivo PCM of cavitation events induced by shockwave treatment. (a) Representative PCM image of cavitation signals at 116 μs after shockwave pulse #520. (b) Ensembled PCM images of cavitation events induced by 30 shockwave pulses (#520 – #550). (c) Scatter plot of cavitation centers induced by the 30 shockwave pulses. (d) The overlay image with the cavitation centers superimposed on top of the PAT image of the vascular injury.

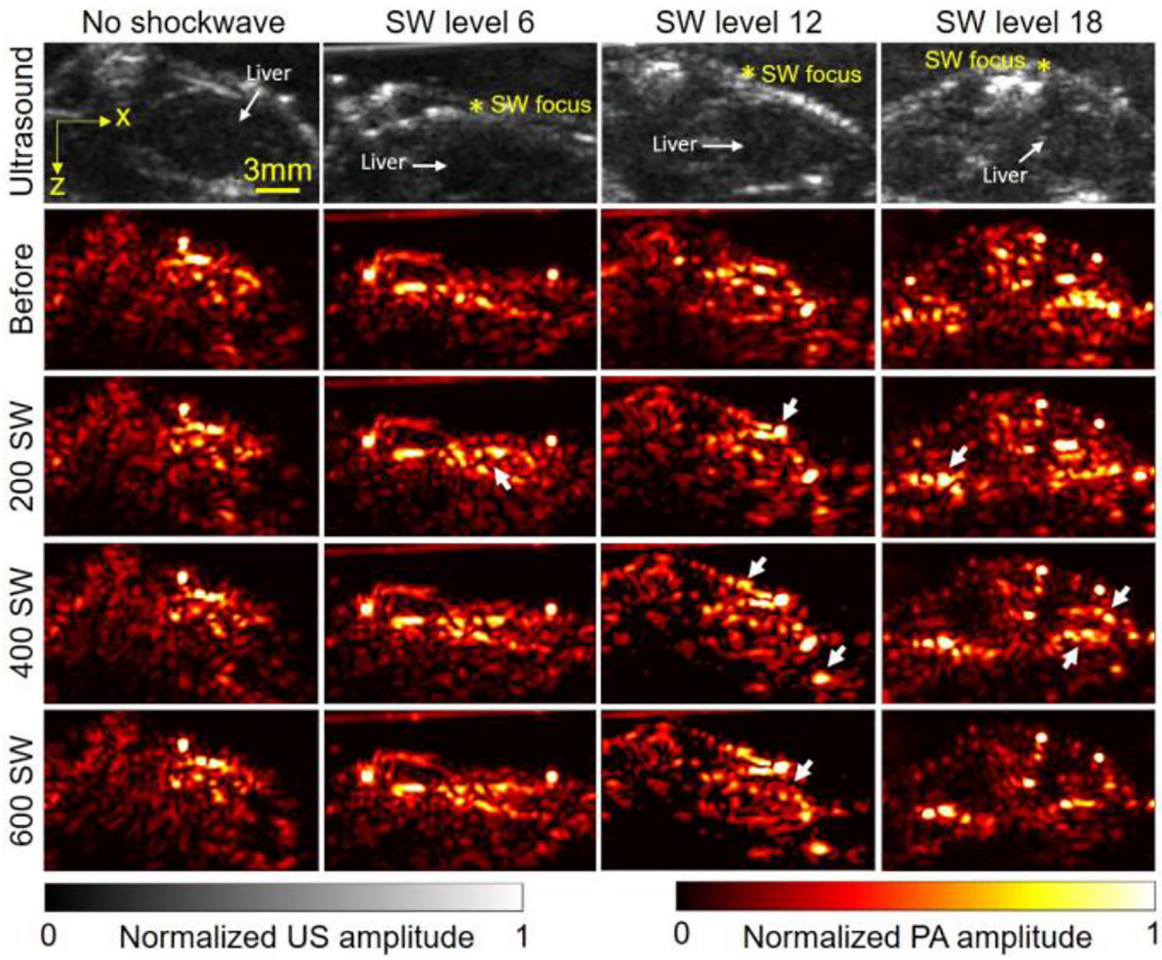

Fig. 9.

PAT of tissue injury at different SW pulse energy levels. Each column shows the PAT images at multiple time points at the SW pulse energy level of 0, 6, 12 and 18. The white arrows indicate the identified hemorrhage sites.

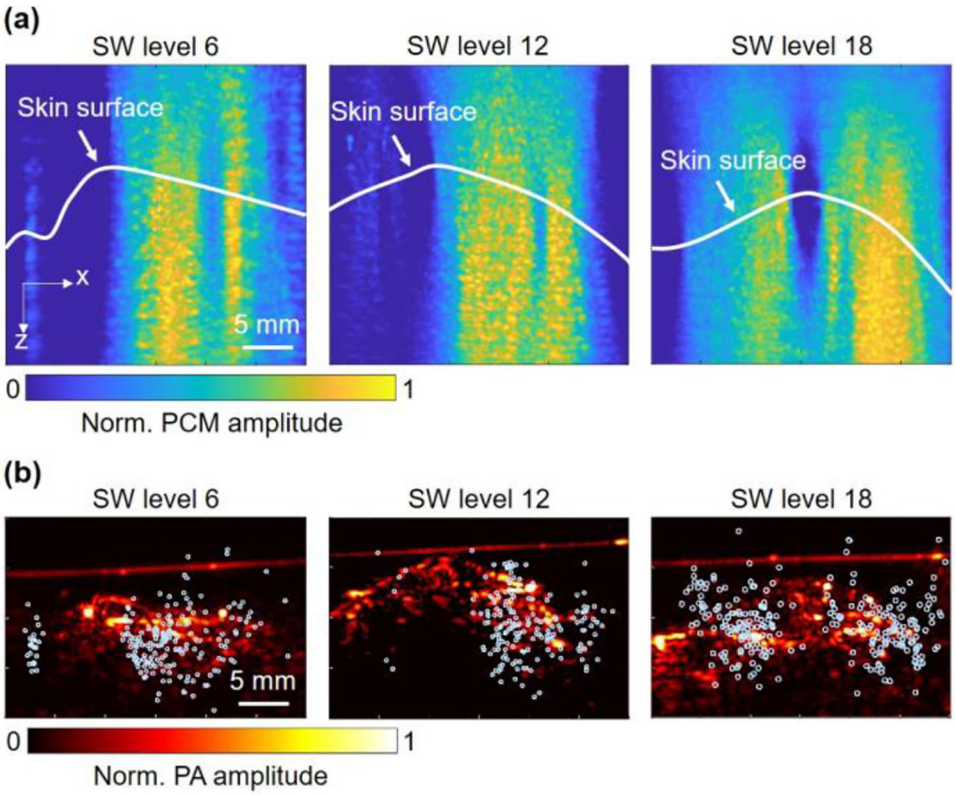

Fig. 10.

Reconstructed cavitation events at different SW pulse energy levels. (a) Ensembled PCM images of cavitation events induced by 13 SW pulses at the energy level of 6, 12 and 18, respectively. (b) The overlay images of the cavitation centers superimposed on top of the PAT images.